Highly active and durable FeNiCo oxyhydroxide OER electrocatalysts derived from fluoride precursors

*Masahiro Nishimoto, Sho Kitano, [†] Damian Kowalski, [†] Yoshitaka Aoki[†] and Hiroki Habazaki[†,]**

Graduate School of Chemical Sciences and Engineering, Hokkaido University, North 13, West 8, Sapporo, Hokkaido 060-8628, Japan

[†]Division of Applied Chemistry, Faculty of Engineering, Hokkaido University, North 13, West 8, Sapporo, Hokkaido 060-8628, Japan

*Corresponding author: habazaki@eng.hokudai.ac.jp (Hiroki Habazaki)

KEYWORDS: electrocatalyst, oxygen evolution reaction, FeNiCo alloy, anodizing, fluoride

ABSTRACT

Developing highly active and durable electrocatalysts, consisting of earth-abundant elements, for oxygen evolution reaction (OER) is pivotal for large-scale water splitting for hydrogen production. Herein, we report that the commercially available FeNiCo alloy can be converted to a highly active electrocatalyst for OER through galvanostatic anodizing in a fluoride-containing ethylene glycol electrolyte. Anodizing of the alloy develops a porous film consisting of the $(FeNiCo)F_2$ phase, which is readily converted to a highly active porous oxyhydroxide during anodic polarization in a KOH electrolyte. The anodized alloy exhibits high activity and high durability for OER with the overpotential as low as 0.26 V at a current density of 10 mA cm^{-2}. The present study demonstrates that a simple and cost-effective anodizing process can be used to form a highly active OER electrode from a low-cost, practical, iron-based alloy. In addition, we found that fluorides containing Fe, Ni, and Co are excellent precursors for the formation of oxyhydroxides exhibiting high OER activity and durability.

Introduction

Electrochemical water stripping for producing hydrogen is attracting increasing attention during the transition from a fossil fuel-dependent society to a renewable energy-based society, owing to hydrogen's promising potential as a renewable energy carrier for energy conversion and storage. Several electrochemical devices, such as solid oxide electrolysis cells,[1] polymer electrolyte electrolysis cells,[2-3] alkaline electrolysis cells,[2-3] and photoelectrochemical cells,[4] are currently used to produce hydrogen. Alkaline water-splitting devices are cheap to produce hydrogen;

however, they are currently limited by their low energy conversion efficiency. Electrocatalysts exhibiting greater OER efficiency are required to increase hydrogen production efficiency, as current electrocatalysts exhibit the slow OER kinetics in alkaline media at temperatures below 100 °C.

Hydrogen production through alkaline electrolysis has been conducted for more than 40 years. Traditionally, porous Ni and Ni-based alloy electrodes have been utilized for the OER owing to their relatively high activity and high resistance to corrosion in alkaline media.[5-6] Electrocatalysts for polymer electrolyte electrolysis in acidic environments are limited to noble metal elements, such as Pt, Ru, and Ir, which exhibit high activity and durability. In contrast, alkaline water splitting is achievable using low-cost electrocatalysts free from noble metals.

The use of earth-abundant electrocatalysts is crucial for the large-scale production of hydrogen by water splitting. Fe-, Co-, and Ni-based electrocatalysts have been extensively investigated, and these studies are well summarized in recent reviews.[7-11] Several studies have confirmed that the addition of Fe to Ni- and Co-based electrocatalysts significantly enhances the OER activity, suggesting the critical importance of Fe to the OER.[10, 12-16] Although crystalline transition metal oxides and hydroxides are the majority of studies, highly active amorphous oxide electrocatalysts based on Fe, Co, and Ni elements have also been reported.[17-20]

OER electrode fabrication is generally realized through the binding of a powdered active electrocatalyst to the surface of a current collector with a polymeric binder. However, this fabrication route can potentially increase the electrode's electrical resistance, bury active sites, and limit mass transport. Conductive additives, such as carbon black, are often added to the binder to ensure an electrical conduction route to electrocatalyst powders in electrodes exhibiting poor electronic conductivity.[21] Conventional carbon additives are readily consumed under alkaline OER

conditions, although novel oxidation-resistant carbon materials have recently been reported.[22] Thus, the development of highly active and durable OER electrodes without binders and conductive additives is desirable for their practical application in water splitting.

Electrodeposition of OER active materials on a current collector is a promising approach for the binder-free fabrication of electrodes. Lu et al. reported the electrodeposition of hierarchically porous amorphous Ni-Fe composite nanosheets directly onto a microporous Ni foam current collector, with the electrode exhibiting an OER onset potential as low as 200 mV.[23] However, composite nanosheets deposited on a current collector through electrodeposition still face adhesion issues. More recently, the direct conversion of metal or alloy surfaces to active species has attracted particular interest. Zhang et al. reported the formation of a highly active Ni-Fe hydroxide/Ni foam electrode through hydrothermal surface oxidation of the Ni foam, which was then followed by soaking in an $Fe(NO_3)_3$ aqueous solution to facilitate the incorporation of Fe species.[24] Fan et al. demonstrated the formation of highly active nanosheets by anodizing electrodeposited FeCoNi alloys.[25] Anodizing of metals and alloys is an established method of forming porous surface layers directly on metallic substrates.[26-27] Recently, the activation of stainless steels for the OER has been reported.[28-35] In this application, low overpotential for the OER and sufficient durability have been reported; however, under alkaline OER conditions, the dissolution of chromate occurs from the stainless steels, which contain, typically 16–18 mass% Cr. Thus, chromium-free steels are more suitable for use as OER electrodes. Ni-Fe alloy (Ni42 steel) containing 42 mass% Ni was activated and exhibited an OER onset overpotential of 215 mV at pH 14, establishing it as a promising candidate for OER electrodes.[36-37]

In this study, we investigated a practical FeNiCo alloy, named Kovar, for its potential use as a highly active and durable OER electrode. The alloy was activated through galvanostatic anodizing

in a fluoride-containing ethylene glycol electrolyte. Then, the OER activity and durability were examined in a 1.0 mol dm^{-3} KOH electrolyte. The anodizing of the alloy developed a fluoride-based porous layer, which was readily converted to a highly active, poorly crystalline, oxyhydroxide layer in the KOH electrolyte. This study demonstrates that FeNiCo fluoride is a suitable precursor for the formation of oxyhydroxide electrocatalysts exhibiting high OER activity.

Experimental

A commercial FeNiCo alloy (Kovar or ASTM F-15 alloy, Nilaco Corporation, Japan), with a composition of 29.72 wt% Ni, 16.28 wt% Co, 0.17 wt% Mn, 0.20 wt% Si with Fe balanced, was used in this study. Prior to anodizing, the alloy sheet of 0.3 mm thickness was ultrasonically degreased in acetone for 10 min. Porous anodic layers were formed by anodizing the alloy at a constant current density of 50 mA cm^{-2} in ethylene glycol electrolyte containing 0.54 mol dm^{-3} NH_4F and 2.5 mol dm^{-3} H_2O at 293 K for predetermined periods of time. A two-electrode cell with a Pt counter electrode was used for anodizing. The anodized specimens were washed in ethylene glycol and dried in the air, followed by annealing in the air at 373 K for 1 h.

The OER activity was evaluated through cyclic voltammetry (CV) measurements performed in a 1.0 mol dm^{-3} KOH electrolyte at room temperature using a computer-controlled electrochemical system (Princeton Applied Research, Versastat4) with a frequency response analyzer. The CV curves were obtained in a potential range between 1.1 and 1.8 V vs RHE using a three-electrode cell with a Pt counter electrode and a Hg/HgO/1 mol dm^{-3} KOH reference electrode at a potential sweep rate of 10 mV s^{-1}. For iR compensation, the conductivity of electrolyte solution was determined by electrochemical impedance spectroscopy in the frequency range between 1 Hz and 10 kHz at an amplitude of 5 mV at 1.55 V vs RHE. The electrochemical surface area (ECSA) of

the electrodes was estimated by CV measurements over the potential range of 0.74 and 0.88 V vs RHE at several potential sweep rates between 10 and 100 mV s^{-1} in 1.0 mol dm^{-3} KOH electrolyte. The durability of the electrodes was investigated by applying a constant current density of 100 mA cm^{-2} for 200 h.

The surface morphology of electrodes was examined using scanning electron microscopy (SEM) (ZEISS, Sigma-500) operated at 1.5 kV. The thickness of the porous layer was determined through SEM analysis of the fractured cross-sections. Cross-sections were also analyzed using a scanning transmission electron microscope (JEOL, JEM-ARM200F) with energy-dispersive X-ray spectroscopy (EDS) facilities. The electron-transparent sections were imaged using a focused ion beam (FIB) system (Hitachi, FB-2100). The surface composition and chemical state of the individual elements were examined by X-ray photoelectron spectroscopy (XPS) (JEOL, JPS-9200) utilizing Mg Kα ($h\nu$ = 1486.6 eV) radiation. Phases in the electrodes were identified by X-ray diffraction (XRD) utilizing Cu Kα radiation (λ = 0.15418 nm). Herein, α-2θ mode measurements, where $\alpha = 2°$, were utilized to enhance the reflections from the porous surface layer. Phases in the anodized electrodes before and after immersion or polarization in the KOH electrolyte were also identified by Raman spectroscopy measurements (Horiba Scientific, XploRA) using a 532 nm laser beam.

Results and Discussion

Characterization of the anodized alloy

Scanning electron micrographs of the FeNiCo alloy anodized for 70, 250, 400, and 7200 s reveal the formation of a porous layer on the alloy surface (**Figure S1**). The thickness of the porous layer

increases almost linearly with anodizing time with a corresponding growth rate of 1.07 nm s^{-1} (**Figure S2**). As discussed later, the highest OER activity was exhibited in the alloy anodized for 250 s. Thus, a relatively short anodizing time was sufficient to obtain a highly active OER electrode, although previous studies have reported a considerably longer anodizing time of 8 h for similar FeCoNi alloys.[25]

Phases in the porous layer were examined by XRD and selected area electron diffraction (SAED) patterns obtained from the TEM cross-section (**Figure 1**). The XRD pattern of the as-received alloy reveals three reflections at 42°, 51°, and 74°, corresponding to the 111, 200, and 220 reflections of the face-centered cubic phase, respectively (**Figure 1a**). An additional weak reflection was recorded at 34° in all anodized specimens. This reflection corresponds to the 101 reflection of the difluoride of Fe, Ni, and Co, which has a Rutile-type phase arrangement. The SAED pattern of the porous layer, as shown in the inset of **Figure 1b**, clearly indicates the presence of the Rutile-type $(FeNiCo)F_2$ phase.

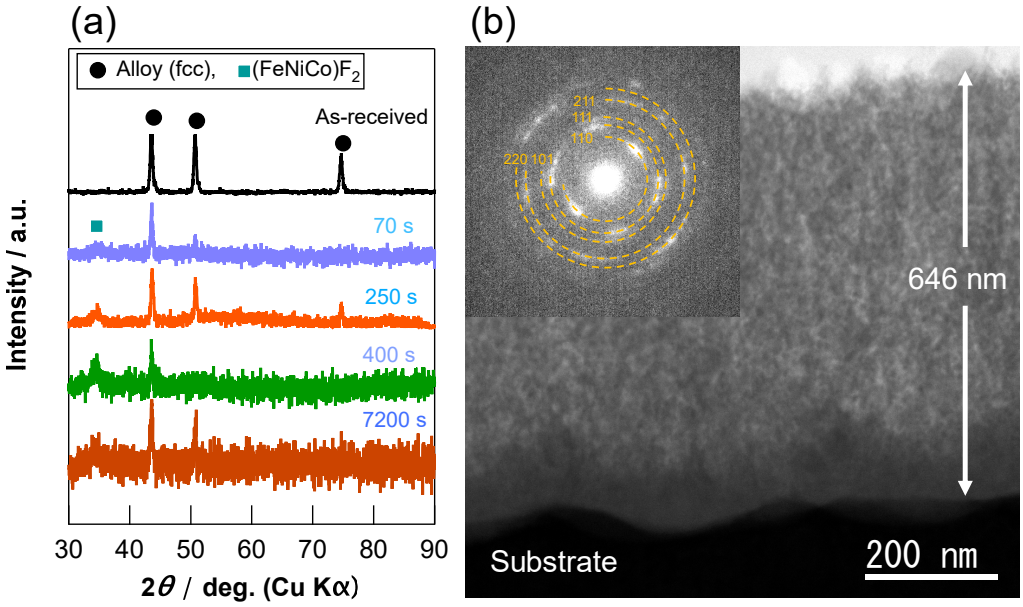

Figure 1. (a) XRD patterns of the FeNiCo alloy as-received and anodized for 70, 250, 400, and 7200 s; (b) scanning transmission electron micrograph of an FIB-cross-section; and (c) selected area electron diffraction (SAED) pattern of the porous layer for the alloy anodized for 250 s.

Figure 2 shows the STEM/EDS elemental mapping of the cross-section of the alloy anodized for 250 s. It was observed that the alloy's constituent elements were homogeneously distributed throughout the porous layer formed during anodizing. Since the anodizing electrolyte contains fluoride, fluorine species were significantly incorporated into the porous layer, developing the $(FeNiCo)F_2$ phase. The composition of the middle section of the porous layer is listed in **Table 1**. It was clear that the fluorine content in the anodic film was considerably higher than that of oxygen. Thus, it was confirmed that fluoride-rich oxyfluoride possessing a crystalline Rutile-type phase of $(FeNiCo)F_2$ was developed through anodizing. The majority of constituent elements were homogeneously distributed throughout the porous layer, except in the case of fluoride enrichment, which occurred immediately above the alloy/porous layer interface (**Figure 2e**). Fluoride enrichment is associated with an increased migration rate of fluoride ions than oxide ions toward the alloy substrate within the barrier layer, located between the alloy substrate and the porous layer.[38] Fluoride ion migration occurring at approximately twice the rate of oxide ion migration in the anodically formed TiO_2 and Ta_2O_5 films has been previously reported.[39-40]

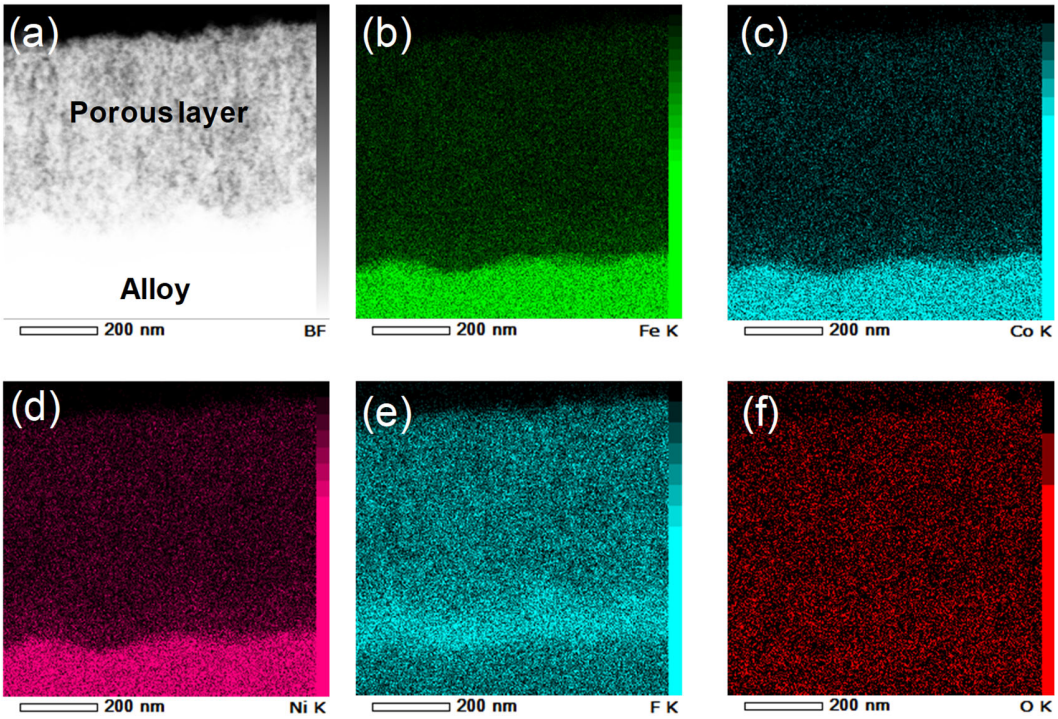

Figure 2. STEM/EDS elemental mapping of the FIB-cross-section of the FeNiCo alloy anodized for 250 s: (a) HAADF image, (b) Fe, (c) Co, (d) Ni, (e) F and (f) O elemental mapping.

Table 1. EDS composition of the porous layer formed through anodizing of the FeNiCo alloy for 250 s before and after the five CV cycles for OER in KOH electrolyte.

Specimen	Composition (at%)				
	Fe	Ni	Co	F	O
As-anodized	16.0	12.4	3.8	57.7	10.1
After OER	17.0	14.6	4.2	3.2	60.9
Substrate	55.3	28.2	16.5	-	-

OER characteristics

The OER characteristics of the anodized alloy were examined in a 1.0 mol dm^{-3} KOH electrolyte. The electric double-layer capacitance was determined to estimate the ECSA through CV measurements (**Figure S3**). The current density in the CV curves of the alloy anodized for ≥ 250 s is larger than that of the alloy anodized for 70 s. The anodic current density at 0.81 V vs RHE exhibits a linear relationship with the potential sweep rate (**Figure 3a**); from this linear correlation, the electric double-layer capacitance, C_{DL}, was estimated using the slope and the following equation:

$$i_a = \nu C_{DL}, \qquad (1)$$

where ν is the potential sweep rate.[41] Assuming a specific capacitance of 0.040 mF cm^{-2},[41] the roughness factor (RF) for each electrode was estimated and summarized in **Table 2**. Although the thickness of the porous layer increases with anodizing time, the RF does not exhibit a similar increase; the RF enlargement is limited to approximately twice that of the as-received alloy. The limited increase in RF, regardless of the thickness of the porous layer, may result from the poor electrical conductivity of the porous layer formed through anodizing.

Table 2. Changes in the capacitance, roughness factor (RF), Tafel slope, and OER onset potential of the FeNiCo alloy under varying anodizing periods.

Anodizing time (s)	Capacitance (mF cm^{-2})	RF	Tafel slope (mV $decade^{-1}$)	Onset potential (V vs RHE)
0	0.25	6.3	40	1.572
70	0.20	5.0	47	1.511
250	0.47	11.8	42	1.490
400	0.42	10.5	41	1.494

7200	0.53	13.2	35	1.502

The CV curves were then measured to evaluate OER activity. **Figure 3b** shows the CV curves of the alloy anodized for 250 s. The OER current remained almost unchanged throughout the five cycles, while the onset OER potential, defined as the potential of 10 mA cm^{-2}, had a value of 1.490 V vs RHE. CV curves that were independent of the CV cycles were obtained for the alloys subjected to different anodizing periods as well as the as-received alloy. **Figure 3c** shows the linear sweep voltammetry (LSV) curves of the alloy as-received and anodized for different periods. The LSV curves disclose significantly enhanced OER activity through anodizing. The onset potential of the as-received alloy was 1.572 V vs RHE, whereas each of the anodized alloy electrodes exhibited a less noble shift of the onset potential of more than 60 mV. It was observed that the alloy anodized for 250 s exhibited the lowest onset potential (**Table 2**).

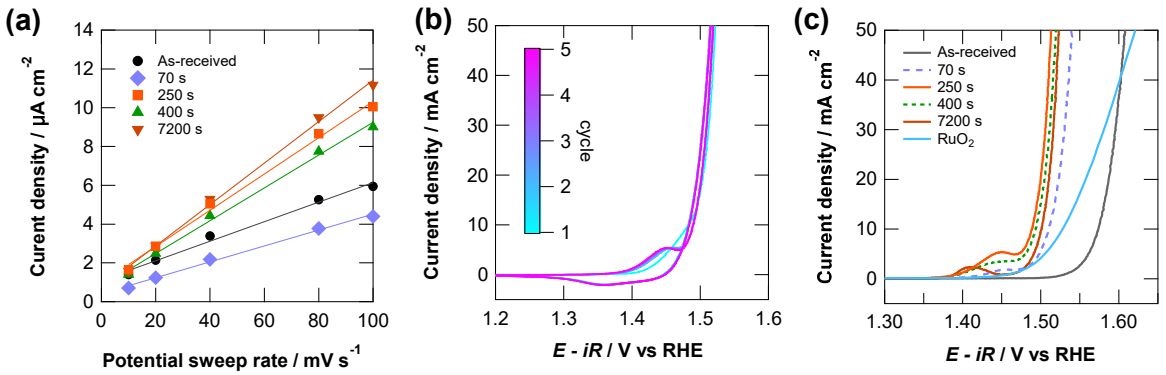

Figure 3. (a) Change in the anodic current density at 810 mV vs RHE in the CV curves with potential sweep rate, (b) CV curves of the alloy anodized for 250 s for the OER during five cycles, and (c) LSV curves of the alloy as-received and anodized for several periods for OER.

The Tafel slope is shown in **Figure 4a** and **Table 2** and does not change significantly with the anodizing time. The Tafel slope is in the range of 35–47 mV dec^{1}; these relatively small values are beneficial for reducing the overpotential at high current densities. The reaction mechanism for the OER is rather complex, and the followings are the most widely accepted elementary steps in alkaline media:[6, 42-43]

First step:

$$M + OH^- \rightarrow MOH_{ads} + e^- \quad (1)$$

Second step:

$$MOH_{ads} + OH^- \rightarrow MO_{ads} + H_2O + e^- \quad (2)$$

or

$$MOH_{ads} + MOH_{ads} \rightarrow MO_{ads} + M + H_2O \quad (3)$$

Third step:

$$2MO_{ads} \rightarrow 2M + O_2(g) \quad (4)$$

In the above mechanism, it has been reported that Tafel slopes of 120, 40, 30, and 15 mV dec^{-1} should be detected when the overall reaction rate is controlled by steps (1), (2), (3), and (4), respectively.[42] Thus, it is suggested from the Tafel slopes that step (2) controls the overall rate of the OER on the as-received and anodized FeCoNi electrodes.

Le Formal et al. recently reported the OER activity of FeNiCo alloys of various compositions in a KOH electrolyte.[44] They used an as-polished alloy, which was not subjected to anodizing. The OER activity was largely dependent on the alloy composition, and the overpotential remained above 300 mV at 10 mA cm^{-2} even at the highest activity. It can, therefore, be said that the

anodized FeNiCo alloys in this study exhibit greater OER activity than FeNiCo alloys of any practical composition. The findings in this study indicate that anodizing is a simple and effective process for converting commercial, low-cost, iron-based alloys into highly active OER electrodes.

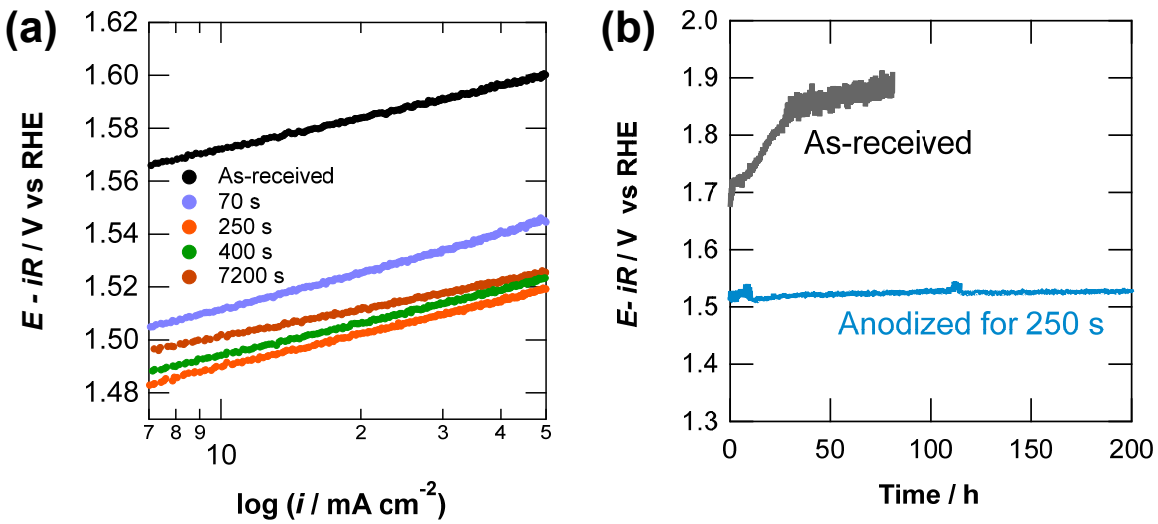

Figure 4. (a) Tafel plots of the alloy as-received and anodized for several periods and (b) the change in potential with time during the durability test at 100 mA cm^{-2}.

The durability of the highly active, anodized FeNiCo alloy electrode was also examined at a constant current density of 100 mA cm^{-2} (**Figure 4b**). The potential of the as-received FeNiCo alloy gradually shifted toward a noble direction, suggesting a degradation of the electrode. In contrast, a relatively stable potential of ~1.51 V vs RHE was maintained during the durability test up to 200 h, confirming the high durability of the anodized alloy electrode. The strong adhesion of the porous layer formed through anodizing is one factor that contributes to its high durability. The surface morphologys of the electrode did not change siginificantly even after the durability test, as shown inFigure S4.

It is worth comparing the OER activity of the present anodized FeNiCo electrode with the previously reported Ni- and Co-based electrocatalysts (**Table 3**). The overpotential at 10 mA cm−2 of the anodized FeNiCo electrode studied in this study is relatively low compared with the reported electrocatalysts. Furthermore, the Tafel slope in the present study is comparable to those of the layered double hydroxides (LDHs). Therefore, the short-period and straightforward anodizing of FeNiCo alloy is an efficient approach to fabricating a highly active OER electrode.

Table 3. Comparison of the overpotential and Tafel slope of the various Fe-, Ni-, and Co-based electrocatalysts in 1.0 mol dm^{-3} KOH electrolyte.

Sample	η (mV) at 10 mA cm^{-2}	Tafel slope (mV dec^{-1})
Anodized FeNiCo (This study)	260	42
Anodized Ni-11.8%Fe [45]	260	53
Activated 316 stainless steel [30]	254	41
$Ni_{0.83}Fe_{0.17}(OH)_2$ nonosheet [46]	245	61
NiFe-LDH/CNT [12]	247	31
Holey $Ni(OH)_2$ [47]	335	65
Exfoliated NiFe LDH [48]	302	40
Exfoliated NiCo LDH [48]	334	41
Exfoliated CoCO LDH [48]	307	45
$Ni_{0.75}Co_{0.25}O_x$ [49]	345	33
CoO_x [49]	423	42
Ni_2P/NF [50]	290	47
CoP films [50]	345	47
IrO_2 [50]	338	47

OER active species

To understand the high OER activity mechanisms of the anodized FeNiCo electrodes, XPS analysis of the electrode was performed after anodizing, five CV cycles, and durability tests. **Figure 5** shows the XPS spectra of Fe $2p_{3/2}$, Ni $2p_{3/2}$, Co $2p_{3/2}$, O 1s, and F 1s electrons. The peak binding energies of Fe $2p_{3/2}$, Ni $2p_{3/2}$, and Co $2p_{3/2}$ spectra shifted toward lower binding energies after the five CV cycles and durability tests than those obtained from the as-anodized electrode. This binding energy shift is associated with converting the fluoride-rich oxyfluoride to oxyhydroxide with minimal fluoride content.[51] The presence of more electronegative fluoride anions than oxide anions causes higher binding energy shifts of the Fe, Ni, and Co peaks. After five CV cycles and the durability test, the peak binding energies suggested the presence of Fe^{3+}, Ni^{2+}, and Co^{3+} species.[52] The broader peaks of Fe and Ni $2p_{3/2}$ electrons for the anodized electrode in comparison with those after OER are probably due to the presence of several species containing fluoride and oxide anions, although the former peaks were not deconvoluted into individual species.

It is observed that the intensity of the O 1s peaks is markedly enhanced (**Figure 5d**), whereas the F 1s peak is significantly reduced after the OER in the KOH electrolyte (**Figure 5e**). The intensities of the Fe $2p_{3/2}$ and Ni $2p_{3/2}$ peaks were reduced after the durability test. In contrast, the Co $2p_{3/2}$ peak increased significantly at the surface, suggesting the preferential dissolution of Ni and Fe at high anodic potentials during the durability tests. The two prominent peaks found at 529.6 and 531.2 eV after the five CV cycles and durability test in the O 1s spectra correspond to O^{2-} and OH^- type oxygen species, respectively. Thus, the dominant anion component after OER is oxyhydroxide, which is derived from the fluoride formed by anodizing.

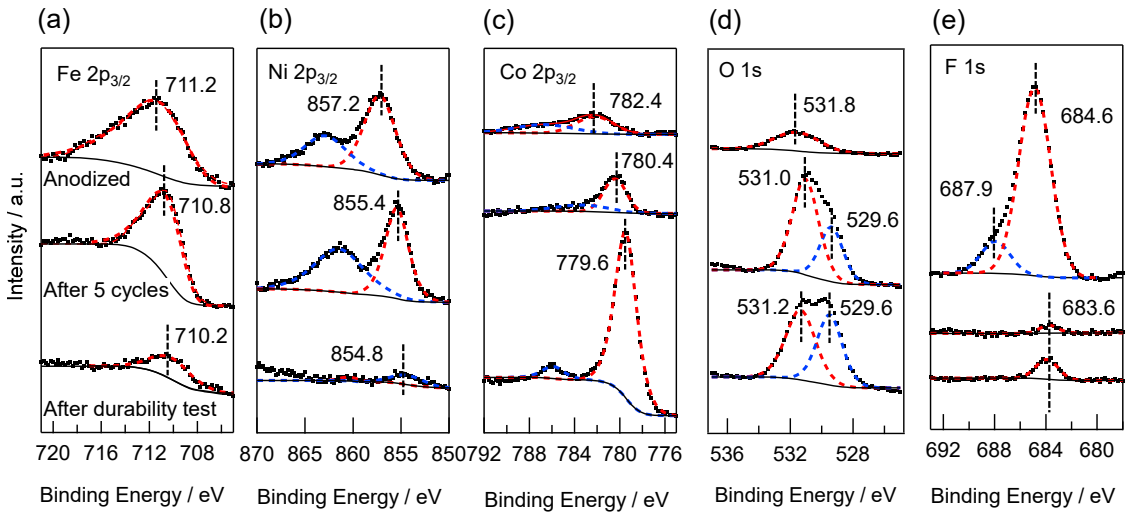

Figure 5. XPS spectra of (a) Fe $2p_{3/2}$, (b) Ni $2p_{3/2}$, (c) Co $2p_{3/2}$, (d) O 1s, and (e) F 1s electrons after anodizing, five cycles of CV, and the durability test in 1.0 mol dm^{-3} KOH electrolyte.

XPS depth profiles were also measured after anodizing, five CV cycles for OER, and the durability test (**Figure 6**). Similar to the results from the EDS analysis (**Figure 2**), the as-anodized electrode was found to be rich in fluorine. At the same time, the oxygen content was low in the porous layer above the alloy substrate (**Figure 6a**). The considerable compositional change occurred after only five CV cycles in the KOH electrolyte. The fluorine content decreased to ~10 at% or less throughout the porous layer, with oxygen becoming the most prominent component (**Figure 6b**). A similar composition was maintained throughout the durability test of 200 h (**Figure 6c**). The sputtering time of the porous layer was reduced from ~90 min to ~50 min after the durability test, suggesting a thinning of the porous layer, although the OER activity remained unchanged. The compositional changes in the constituent alloying elements are summarized in **Figure 6d-6f**. The atomic ratios of Fe, Ni, and Co in the porous layer are similar to those in the alloy substrate post-anodizing, suggesting no preferential dissolution occurs during anodizing in a

fluoride-containing ethylene glycol electrolyte (**Figure 6d**). However, it is found that Ni is enriched, and the Fe content is diminished in the porous layer over the course of five CV cycles in the KOH electrolyte, indicating that preferential dissolution of Fe takes place during the conversion of the fluoride phase formed during anodizing to oxyhydroxide. It was observed that Co enrichment also occurred in the porous layer during the durability test, particularly at the outermost surface. The Ni to Fe ratio remained almost unchanged throughout the durability tests. Thus, Co enrichment in the porous layer appears to result from the dissolution of Fe and Ni in this layer at a comparable rate. The dissolution rate of Fe and Ni is rather low, resulting in a marked enrichment of Co only at the outermost surface of the electrode.

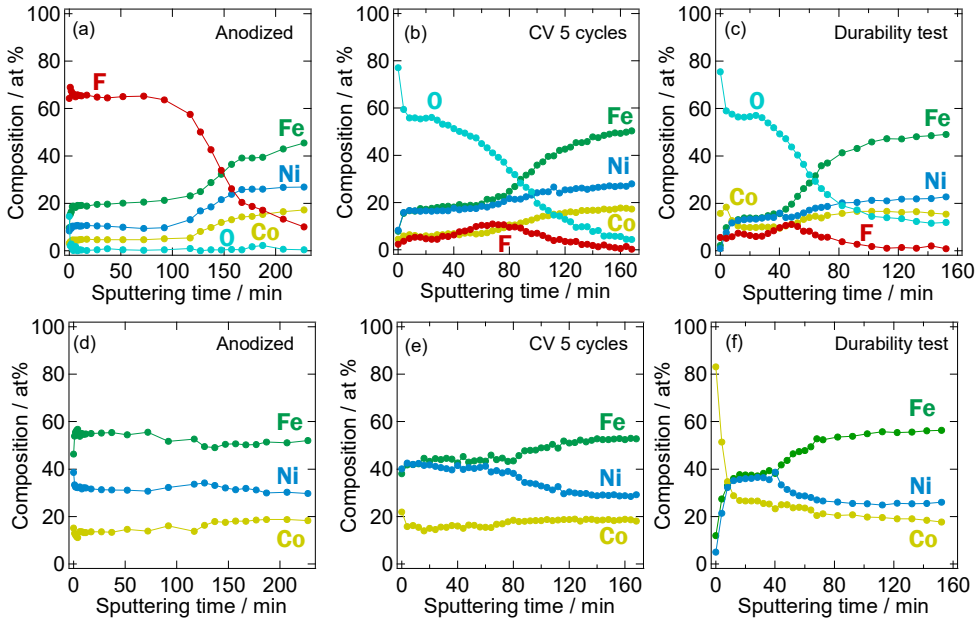

Figure 6. XPS depth profiles of the FeNiCo electrodes (a, d) as-anodized, (b, e) after five CV cycles and (c, f) after the durability test.

After five CV cycles, the phases and composition of the porous layers were examined using FIB/STEM analysis. **Figure 7a** shows the remaining porous layer (~500 nm thickness) on the alloy

substrate, which appears at the bottom of the micrograph. The porous layer is highly adherent to the substrate throughout the FIB cross-section. The selected area diffraction pattern of the central area of the porous layer (inset of **Figure 7a**) reveals weak Debye–Scherrer rings that correspond to d spacings of 0.26 and 0.15 nm. These spacings can be assigned to the 100 and 110 reflections of β-NiOOH (JCPDS card No. 6-141), known to be one of the active phases for the OER in alkaline media.[53-55] The EDS elemental maps in **Figures 7c–7g** indicate the homogeneous distribution of each element throughout the porous layer. The quantitative EDS analysis of the porous layer (**Table 1**) indicates a slight enrichment of Ni, a marked increase in O content, and a significant decrease in F content in the porous layer, which is in agreement with the XPS analysis. These findings suggest that the active phase for the OER of the anodized FeNiCo electrodes is poorly crystalline β-NiOOH which is highly doped with Fe and Co.

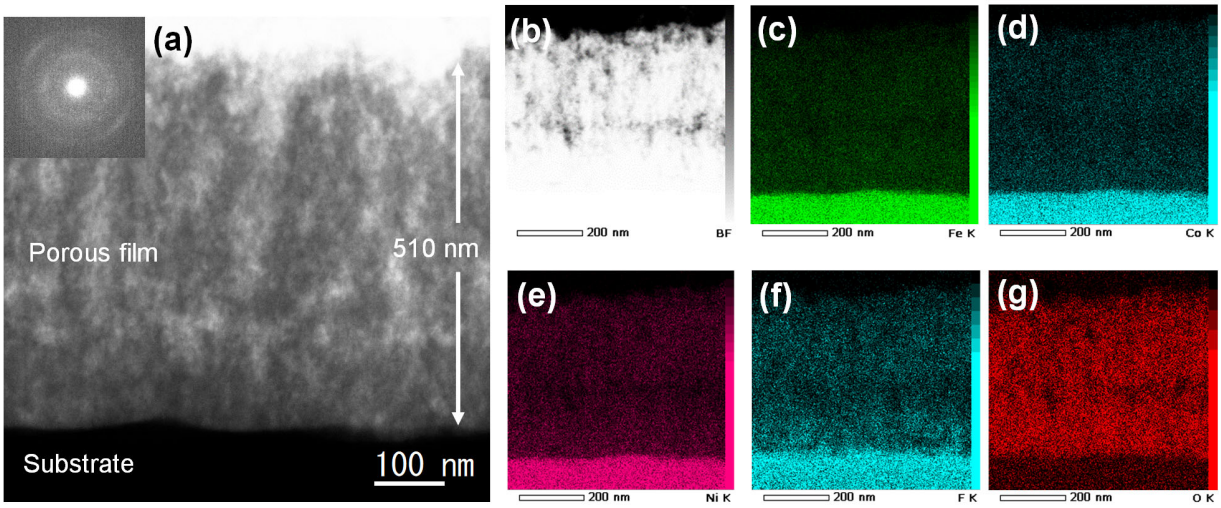

Figure 7. (a) FIB/STEM image and SAED pattern, (b) HAADF and EDS elemental maps of (c) Fe, (d) Ni, (e) Co, (f) F, and (g) O for the anodized FeNiCo electrode after five CV cycles in 1.0 mol dm^{-3} KOH electrolyte.

The transition from fluoride to oxyhydroxide

As discussed previously, the porous fluoride layer formed by anodizing in a fluoride-containing ethylene glycol electrolyte was converted to a highly OER active oxyhydroxide layer during the OER in the KOH electrolyte. Despite such a significant compositional change, the CV cycles of the as-anodized electrode for the OER (Figure 3b) confirmed the high OER activity from the first cycle, and the activity remained unchanged throughout the following cycles. In order to understand the high activity during the initial OER measurements, Raman spectra were measured before and after immersion in KOH electrolyte and after potentiostatic polarization at each potential. The results are shown in **Figure 8a**. The as-anodized electrode exhibits broad peaks at 745 and 545 cm^{-1}, possibly attributed to the A1g and Eg modes of the Rutile-type metal fluorides. The Raman spectrum changed after immersion in the KOH electrolyte for 10 min. The immersed electrode exhibits a peak at 535 cm^{-1} and a shoulder at 470 cm^{-1}, corresponding to the pair of Ni-O vibrations in NiOOH.[13] Thus, the findings indicate that the $(FeNiCo)F_2$ phase (**Figure 8b**) is not stable in the KOH electrolyte and converts to an oxyhydroxide (**Figure 8c**) immediately after immersion.

Similar spectra were also obtained after polarization. The intensity of the two peaks was observed to increase at potentials ≥ 1.45 V vs RHE, higher than that of the redox couple Ni^{2+}/Ni^{3+} (**Figure 3b**). The increased intensity observed at high potentials may indicate the increased formation of the NiOOH phase owing to the oxidation of Ni^{2+} species. Louie et al. examined the Raman spectra of NiOOH with various concentrations of incorporated Fe.[13] The iron concentration exhibits a significant influence on the relative intensity of the two peaks, with the intensity of the lower wavenumber peak being greater than that of the higher wavenumber peak in Fe-free NiOOH. However, the peak intensity of the former decreases with increasing Fe content. The increased intensity of the higher wavenumber peak of the immersed and polarized electrodes in Figure 8

suggests that a comparable amount of Fe is incorporated into NiOOH. This is consistent with the EDS (**Figure 6**) and XPS analyses (**Table 1**).

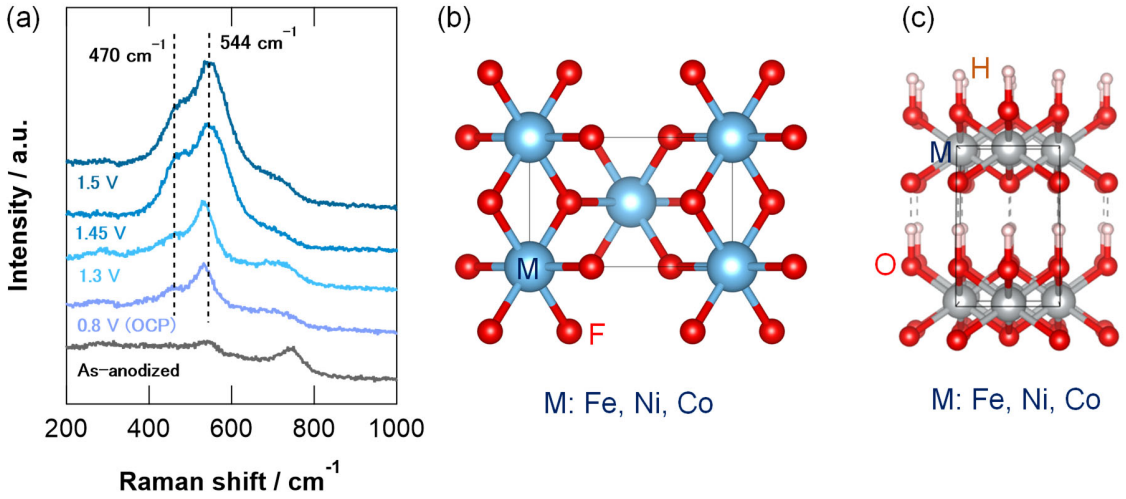

Figure 8. (a) Raman spectra of anodized alloy electrodes before and after immersion or polarization at several potentials in 1.0 mol dm^{-3} KOH electrolyte for 10 min, and the crystal structures of (b) $(FeNiCo)F_2$ and (c) (FeNiCo)OOH.

Recently, Yamada et al. reported that Ni-Fe electrodeposited electrodes exhibit markedly enhanced OER activity through anodizing in a fluoride-containing ethylene glycol electrolyte.[45] The OER activity of the anodized Ni-Fe electrodes is dependent on the alloy composition, and the Ni-rich (Ni-11.8 at%) Fe alloy exhibited the highest OER activity. However, the activation occurs gradually during potential cycling over 50 cycles between 1.1 and 1.8 V vs RHE in 1.0 mol dm^{-3} KOH electrolyte, in contrast to the immediate activation in the present anodized FeNiCo electrode. The significantly different activation behavior of the anodized FeNiCo and Ni-rich Ni-Fe

electrodes is likely a result of the differing alloy compositions. The Ni-rich fluoride should exhibit greater stability and resistance to conversion to oxyhydroxide in the KOH electrolyte than fluorides containing large concentrations of Fe and Co, resulting in a reduction in the OER activation rate of the former fluoride phase.

Recently, highly active Fe-doped NiOOH electrocatalysts for the OER have been prepared from precursors of amorphous Fe-doped nickel phosphate,[56] Ni_2P nanocrystals,[57] metal-organic frameworks,[58] and $NiSe_2$ nano-dendrites.[59] The work presented in this study confirms that the $(FeNiCo)F_2$ formed through anodizing is also a valuable precursor for the preparation of highly active oxyhydroxides for the OER. The advantages of this method include the formation of a porous fluoride layer directly on a metal substrate, which can be used as a current collector, and the ready and rapid conversion to the OER active poorly crystalline (FeNiCo)OOH configuration. Thus, anodizing iron-based alloys containing Ni and Co is a promising approach for fabricating practical OER electrodes exhibiting high activity and durability.

Conclusions

Highly active and durable OER electrodes were successfully prepared by the simple and cost-effective anodizing of commercially available FeNiCo bulk alloys in a fluoride-containing ethylene glycol electrolyte. Anodizing produces a porous layer consisting of a crystalline, Rutile-type, $(FeNiCo)F_2$ phase, which is immediately converted to a poorly crystalline oxyhydroxide in the KOH electrolyte. The anodized FeNiCo electrode exhibits an overpotential as low as 0.26 V at 10 mA cm^{-2}, a Tafel slope of ~40 mV dec^{-1}, and acceptable durability in alkaline media. Thus, the porous metal fluoride formed by anodizing FeNiCo alloy is a promising precursor for developing a highly active OER electrocatalyst. Furthermore, the anodizing of iron-based alloys

is a practical approach for activating low-cost commercial transition metal alloys, i.e., free from noble metals, for the OER.

ASSOCIATED CONTENT

Supporting Information.

The Supporting Information is available free of charge at https://pubs.acs.org/doi/....

Scanning electron micrographs of the FeNiCo alloy anodized for different periods of time, change in the porous layer thickness with anodizing time, CV curves of the alloy anodized for different periods of time for ECSA evaluation, scanning electron micrographs of the anodized FeNiCo alloy after OER (PDF).

AUTHOR INFORMATION

Corresponding Author

Hiroki Habazaki - Division of Applied Chemistry, Faculty of Engineering, Hokkaido University, Sapporo, Hokkaido 060-8628, Japan; orcid.org/0000-0002-7172-8811; Email: habazaki@eng.hokudai.ac.jp

Authors

Masahiro Nishimoto – Graduate School of Chemical Sciences and Engineering, Hokkaido University, Sapporo, Hokkaido 060-8628, Japan

Sho Kitano, Division of Applied Chemistry, Faculty of Engineering, Hokkaido University, Sapporo, Hokkaido 060-8628, Japan; orcid.org/0000-0001-5487-4369

Damian Kowalski, Division of Applied Chemistry, Faculty of Engineering, Hokkaido University, Sapporo, Hokkaido 060-8628, Japan; orcid.org/0000-0002-5222-7827

Yoshitaka Aoki, Division of Applied Chemistry, Faculty of Engineering, Hokkaido University, Sapporo, Hokkaido 060-8628, Japan; orcid.org/0000-0001-5614-1636

Notes

The authors declare no competing financial interest.

ACKNOWLEDGMENT

This work was supported in part by JSPS KAKENHI Grant Number 19H02469 and the University Research Aid from the JFE 21st Century Foundation. Apart of this work was conducted at the Promotion Office for the Nanotechnology Collaboration and Laboratory of XPS analysis, Hokkaido University, supported by "Nanotechnology Platform" Program of the Ministry of Education, Culture, Sports, Science and Technology (MEXT), Japan.

REFERENCES

1. Pandiyan, A.; Uthayakumar, A.; Subrayan, R.; Cha, S. W.; Moorthy, S. B. K., Review of solid oxide electrolysis cells: a clean energy strategy for hydrogen generation. *Nanomater Energy* **2019,** *8* (1), 2-22, DOI 10.1680/jnaen.18.00009.

2. Sapountzi, F. M.; Gracia, J. M.; Weststrate, C. J.; Fredriksson, H. O. A.; Niemantsverdriet, J. W., Electrocatalysts for the generation of hydrogen, oxygen and synthesis gas. *Progress in Energy and Combustion Science* **2017,** *58*, 1-35, DOI 10.1016/j.pecs.2016.09.001.

3. Buttler, A.; Spliethoff, H., Current status of water electrolysis for energy storage, grid balancing and sector coupling via power-to-gas and power-to-liquids: A review. *Renewable and Sustainable Energy Reviews* **2018,** *82*, 2440-2454, DOI 10.1016/j.rser.2017.09.003.

4. Jiang, C.; Moniz, S. J. A.; Wang, A.; Zhang, T.; Tang, J., Photoelectrochemical devices for solar water splitting - materials and challenges. *Chem Soc Rev* **2017,** *46* (15), 4645-4660, DOI 10.1039/c6cs00306k.

5. Hall, D. E., Electrodes for Alkaline Water Electrolysis. *J Electrochem Soc* **1981,** *128* (4), 740-746, DOI 10.1149/1.2127498.

6. Fabbri, E.; Habereder, A.; Waltar, K.; Kötz, R.; Schmidt, T. J., Developments and perspectives of oxide-based catalysts for the oxygen evolution reaction. *Catalysis Science & Technology* **2014,** *4* (11), 3800-3821, DOI 10.1039/C4CY00669K.

7. Han, L.; Dong, S.; Wang, E., Transition-Metal (Co, Ni, and Fe)-Based Electrocatalysts for the Water Oxidation Reaction. *Adv Mater* **2016,** *28* (42), 9266-9291, DOI 10.1002/adma.201602270.

8. Hunter, B. M.; Winkler, J. R.; Gray, H. B., Iron Is the Active Site in Nickel/Iron Water Oxidation Electrocatalysts. *Molecules* **2018,** *23* (4), DOI 10.3390/molecules23040903.

9. Bandal, H.; Reddy, K. K.; Chaugule, A.; Kim, H., Iron-based heterogeneous catalysts for oxygen evolution reaction; change in perspective from activity promoter to active catalyst. *J Power Sources* **2018,** *395*, 106-127, DOI 10.1016/j.jpowsour.2018.05.047.

10. Feng, C.; Faheem, M. B.; Fu, J.; Xiao, Y.; Li, C.; Li, Y., Fe-Based Electrocatalysts for Oxygen Evolution Reaction: Progress and Perspectives. *ACS Catal* **2020,** *10* (7), 4019-4047, DOI 10.1021/acscatal.9b05445.

11. Wang, K.; Wang, X.; Li, Z.; Yang, B.; Ling, M.; Gao, X.; Lu, J.; Shi, Q.; Lei, L.; Wu, G.; Hou, Y., Designing 3d dual transition metal electrocatalysts for oxygen evolution reaction in alkaline electrolyte: Beyond oxides. *Nano Energy* **2020,** *77*, 105162, DOI 10.1016/j.nanoen.2020.105162.

12. Gong, M.; Li, Y.; Wang, H.; Liang, Y.; Wu, J. Z.; Zhou, J.; Wang, J.; Regier, T.; Wei, F.; Dai, H., An advanced Ni-Fe layered double hydroxide electrocatalyst for water oxidation. *J Am Chem Soc* **2013,** *135* (23), 8452-5, DOI 10.1021/ja4027715.

13. Louie, M. W.; Bell, A. T., An investigation of thin-film Ni-Fe oxide catalysts for the electrochemical evolution of oxygen. *J Am Chem Soc* **2013,** *135* (33), 12329-37, DOI 10.1021/ja405351s.

14. Trotochaud, L.; Young, S. L.; Ranney, J. K.; Boettcher, S. W., Nickel-iron oxyhydroxide oxygen-evolution electrocatalysts: the role of intentional and incidental iron incorporation. *J Am Chem Soc* **2014,** *136* (18), 6744-53, DOI 10.1021/ja502379c.

15. Burke, M. S.; Kast, M. G.; Trotochaud, L.; Smith, A. M.; Boettcher, S. W., Cobalt-iron (oxy)hydroxide oxygen evolution electrocatalysts: the role of structure and composition on activity, stability, and mechanism. *J Am Chem Soc* **2015,** *137* (10), 3638-48, DOI 10.1021/jacs.5b00281.

16. Wang, J. Y.; Ji, L. L.; Chen, Z. F., In Situ Rapid Formation of a Nickel-Iron-Based Electrocatalyst for Water Oxidation. *ACS Catal* **2016,** *6* (10), 6987-6992, DOI 10.1021/acscatal.6b01837.

17. Smith, R. D. L.; Prévot, M. S.; Fagan, R. D.; Zhang, Z.; Sedach, P. A.; Siu, M. K. J.; Trudel, S.; Berlinguette, C. P., Photochemical Route for Accessing Amorphous Metal Oxide Materials for Water Oxidation Catalysis. *Science* **2013,** *340* (6128), 60-63, DOI 10.1126/science.1233638.

18. Smith, R. D.; Prevot, M. S.; Fagan, R. D.; Trudel, S.; Berlinguette, C. P., Water oxidation catalysis: electrocatalytic response to metal stoichiometry in amorphous metal oxide films containing iron, cobalt, and nickel. *J Am Chem Soc* **2013,** *135* (31), 11580-6, DOI 10.1021/ja403102j.

19. Kowalski, D.; Kiuchi, H.; Motohashi, T.; Aoki, Y.; Habazaki, H., Activation of Catalytically Active Edge-Sharing Domains in Ca_2FeCoO_5 for Oxygen Evolution Reaction in Highly Alkaline Media. *ACS Appl Mater Interfaces* **2019,** *11* (32), 28823-28829, DOI 10.1021/acsami.9b06854.

20. Sato, Y.; Aoki, Y.; Takase, K.; Kiuchi, H.; Kowalski, D.; Habazaki, H., Highly Durable Oxygen Evolution Reaction Catalyst: Amorphous Oxyhydroxide Derived from Brownmillerite-Type Ca_2FeCoO_5. *ACS Applied Energy Mater* **2020,** *3*, 5269−5276, DOI 10.1021/acsaem.0c00159.

21. Sun, H.; Yan, Z.; Liu, F.; Xu, W.; Cheng, F.; Chen, J., Self-Supported Transition-Metal-Based Electrocatalysts for Hydrogen and Oxygen Evolution. *Adv Mater* **2020,** *32* (3), e1806326, DOI: 10.1002/adma.201806326.

22. Sato, Y.; Kowalski, D.; Aoki, Y.; Habazaki, H., Long-term durability of platelet-type carbon nanofibers for OER and ORR in highly alkaline media. *Appl Catal A: General* **2020,** *597*, 117555, DOI: 10.1016/j.apcata.2020.117555.

23. Lu, X.; Zhao, C., Electrodeposition of hierarchically structured three-dimensional nickel-iron electrodes for efficient oxygen evolution at high current densities. *Nat Commun* **2015,** *6*, 6616, DOI 10.1038/ncomms7616.

24. Zhang, W.; Qi, J.; Liu, K.; Cao, R., A Nickel-Based Integrated Electrode from an Autologous Growth Strategy for Highly Efficient Water Oxidation. *Adv Energy Mater* **2016,** *6* (12), 1502489, DOI 10.1002/aenm.201502489.

25. Fan, J.; Chen, Z.; Shi, H.; Zhao, G., In situ grown, self-supported iron-cobalt-nickel alloy amorphous oxide nanosheets with low overpotential toward water oxidation. *Chem Commun* **2016,** *52* (23), 4290-3, DOI 10.1039/c5cc09699e.

26. Kure, K.; Konno, Y.; Tsuji, E.; Skeldon, P.; Thompson, G. E.; Habazaki, H., Formation of self-organized nanoporous anodic films on Type 304 stainless steel. *Electrochem Commun* **2012,** *21* (0), 1-4, DOI 10.1016/j.elecom.2012.05.003.

27. Habazaki, H.; Konno, Y.; Aoki, Y.; Skeldon, P.; Thompson, G. E., Galvanostatic growth of nanoporous anodic films on iron in ammonium fluoride-ethylene glycol electrolytes with different water contents. *J Phys Chem C* **2010,** *114* (44), 18853-18859, DOI 10.1021/Jp1078136.

28. Zhang, G. R.; Shen, L. L.; Schmatz, P.; Krois, K.; Etzold, B. J. M., Cathodic activated stainless steel mesh as a highly active electrocatalyst for the oxygen evolution reaction with self - healing possibility. *J Energy Chem* **2020,** *49*, 153-160, DOI 10.1016/j.jechem.2020.01.025.

29. Cai, M. Y.; Liu, W. J.; Luo, X.; Chen, C. H.; Pan, R.; Zhang, H. J.; Zhong, M. L., Three-Dimensional and In Situ-Activated Spinel Oxide Nanoporous Clusters Derived from Stainless Steel for Efficient and Durable Water Oxidation. *ACS Appl Mater Interfaces* **2020,** *12* (12), 13971-13981, DOI 10.1021/acsami.0c00701.

30. Todoroki, N.; Wadayama, T., Heterolayered Ni-Fe Hydroxide/Oxide Nanostructures Generated on a Stainless-Steel Substrate for Efficient Alkaline Water Splitting. *ACS Appl Mater Interfaces* **2019,** *11* (47), 44161-44169, DOI 10.1021/acsami.9b14213.

31. Moureaux, F.; Stevens, P.; Toussaint, G.; Chatenet, M., Timely-activated 316L stainless steel: A low cost, durable and active electrode for oxygen evolution reaction in concentrated alkaline environments. *Appl Catal B-Env* **2019,** *258*, 117963, DOI 10.1016/j.apcatb.2019.117963.

32. Anantharaj, S.; Venkatesh, M.; Salunke, A. S.; Simha, T.; Prabu, V.; Kundu, S., High-Performance Oxygen Evolution Anode from Stainless Steel via Controlled Surface Oxidation and Cr Removal. *ACS Sustainable Chem Eng* **2017,** *5* (11), 10072-10083, DOI 10.1021/acssuschemeng.7b02090.

33. Zhong, H. X.; Wang, J.; Meng, F. L.; Zhang, X. B., In Situ Activating Ubiquitous Rust towards Low-Cost, Efficient, Free-Standing, and Recoverable Oxygen Evolution Electrodes. *Angew Chem-Int Edit* **2016,** *55* (34), 9937-9941, DOI 10.1002/anie.201604040.

34. Schafer, H.; Sadaf, S.; Walder, L.; Kuepper, K.; Dinklage, S.; Wollschlager, J.; Schneider, L.; Steinhart, M.; Hardege, J.; Daum, D., Stainless steel made to rust: a robust water-splitting catalyst with benchmark characteristics. *Energy Environ Sci* **2015,** *8* (9), 2685-2697, DOI 10.1039/c5ee01601k.

35. Schafer, H.; Beladi-Mousavi, S. M.; Walder, L.; Wollschlager, J.; Kuschel, O.; Ichilmann, S.; Sadaf, S.; Steinhart, M.; Kupper, K.; Schneider, L., Surface Oxidation of Stainless Steel: Oxygen Evolution Electrocatalysts with High Catalytic Activity. *ACS Catal* **2015,** *5* (4), 2671-2680, DOI 10.1021/acscatal.5b00221.

36. Schäfer, H.; Chevrier, D. M.; Zhang, P.; Stangl, J.; Müller-Buschbaum, K.; Hardege, J. D.; Kuepper, K.; Wollschläger, J.; Krupp, U.; Dühnen, S.; Steinhart, M.; Walder, L.; Sadaf, S.; Schmidt, M., Electro-Oxidation of Ni42 Steel: A Highly Active Bifunctional Electrocatalyst. *Adv Func Mater* **2016,** *26* (35), 6402-6417, DOI 10.1002/adfm.201601581.

37. Schäfer, H.; Chatenet, M., Steel: The Resurrection of a Forgotten Water-Splitting Catalyst. *ACS Energy Letters* **2018,** *3* (3), 574-591, DOI 10.1021/acsenergylett.8b00024.

38. Shahzad, K.; Kowalski, D.; Zhu, C.; Aoki, Y.; Habazaki, H., Ex Situ Evidence for the Role of a Fluoride-Rich Layer Switching the Growth of Nanopores to Nanotubes: A Missing Piece of the Anodizing Puzzle. *ChemElectroChem* **2018,** *5* (4), 610-618, DOI 10.1002/celc.201701103.

39. Shimizu, K.; Kobayashi, K.; Thompson, G. E.; Skeldon, P.; Wood, G. C., The migration of fluoride ions in growing anodic oxide films on tantalum. *J Electrochem Soc* **1997,** *144* (2), 418-423, DOI 10.1149/1.1837425.

40. Habazaki, H.; Fushimi, K.; Shimizu, K.; Skeldon, P.; Thompson, G. E., Fast migration of fluoride ions in growing anodic titanium oxide. *Electrochem Commun* **2007,** *9* (5), 1222-1227, DOI 10.1016/j.elecom.2006.12.023.

41. McCrory, C. C.; Jung, S.; Peters, J. C.; Jaramillo, T. F., Benchmarking heterogeneous electrocatalysts for the oxygen evolution reaction. *J Am Chem Soc* **2013,** *135* (45), 16977-87, DOI 10.1021/ja407115p.

42. Jović, B. M.; Lačnjevac, U. Č.; Jović, V. D.; Krstajić, N. V., Kinetics of the oxygen evolution reaction on NiSn electrodes in alkaline solutions. *J Electroanal Chem* **2015,** *754*, 100-108, DOI 10.1016/j.jelechem.2015.07.013.

43. Anantharaj, S.; Kundu, S.; Noda, S., "The Fe Effect": A review unveiling the critical roles of Fe in enhancing OER activity of Ni and Co based catalysts. *Nano Energy* **2021,** *80*, 105514, DOI 10.1016/j.nanoen.2020.105514.

44. Le Formal, F.; Yerly, L.; Potapova Mensi, E.; Pereira Da Costa, X.; Boudoire, F.; Guijarro, N.; Spodaryk, M.; Züttel, A.; Sivula, K., Influence of Composition on Performance in Metallic Iron–Nickel–Cobalt Ternary Anodes for Alkaline Water Electrolysis. *ACS Catal* **2020,** *10* (20), 12139-12147, DOI 10.1021/acscatal.0c03523.

45. Yamada, N.; Kitano, S.; Yato, Y.; Kowalski, D.; Aoki, Y.; Habazaki, H., In Situ Activation of Anodized Ni–Fe Alloys for the Oxygen Evolution Reaction in Alkaline Media. *ACS Applied Energy Materials* **2020,** *3* (12), 12316-12326, DOI 10.1021/acsaem.0c02362.

46. Zhou, Q.; Chen, Y.; Zhao, G.; Lin, Y.; Yu, Z.; Xu, X.; Wang, X.; Liu, H. K.; Sun, W.; Dou, S. X., Active-Site-Enriched Iron-Doped Nickel/Cobalt Hydroxide Nanosheets for Enhanced Oxygen Evolution Reaction. *ACS Catal* **2018,** *8* (6), 5382-5390, DOI 10.1021/acscatal.8b01332.

47. Kong, X.; Zhang, C.; Hwang, S. Y.; Chen, Q.; Peng, Z., Free-Standing Holey Ni(OH)2 Nanosheets with Enhanced Activity for Water Oxidation. *Small* **2017,** *13* (26), 1700334, DOI 10.1002/smll.201700334.

48. Song, F.; Hu, X., Exfoliation of layered double hydroxides for enhanced oxygen evolution catalysis. *Nat Commun* **2014,** *5* (1), 4477, DOI 10.1038/ncomms5477.

49. Trotochaud, L.; Ranney, J. K.; Williams, K. N.; Boettcher, S. W., Solution-Cast Metal Oxide Thin Film Electrocatalysts for Oxygen Evolution. *J Am Chem Soc* **2012,** *134* (41), 17253-17261, DOI 10.1021/ja307507a.

50. Stern, L.-A.; Feng, L.; Song, F.; Hu, X., Ni_2P as a Janus catalyst for water splitting: the oxygen evolution activity of Ni2P nanoparticles. *Energy Environ Sci* **2015,** *8* (8), 2347-2351, DOI 10.1039/C5EE01155H.

51. Pei, C.; Gu, Y.; Liu, Z.; Yu, X.; Feng, L., Fluoridated Iron-Nickel Layered Double Hydroxide for Enhanced Performance in the Oxygen Evolution Reaction. *ChemSusChem* **2019,** *12* (16), 3849-3855, DOI: 10.1002/cssc.201901153.

52. Lemoine, K.; Lhoste, J.; Hemon-Ribaud, A.; Heidary, N.; Maisonneuve, V.; Guiet, A.; Kornienko, N., Investigation of mixed-metal (oxy)fluorides as a new class of water oxidation electrocatalysts. *Chem Sci* **2019,** *10* (40), 9209-9218, DOI 10.1039/c9sc04027g.

53. Martirez, J. M. P.; Carter, E. A., Unraveling Oxygen Evolution on Iron-Doped β-Nickel Oxyhydroxide: The Key Role of Highly Active Molecular-like Sites. *J Am Chem Soc* **2019,** *141* (1), 693-705, DOI 10.1021/jacs.8b12386.

54. Tkalych, A. J.; Zhuang, H. L. L.; Carter, E. A., A Density Functional plus U Assessment of Oxygen Evolution Reaction Mechanisms on beta-NiOOH. *ACS Catal* **2017,** *7* (8), 5329-5339, DOI 10.1021/acscatal.7b00999.

55. Trotochaud, L.; Young, S. L.; Ranney, J. K.; Boettcher, S. W., Nickel-Iron Oxyhydroxide Oxygen-Evolution Electrocatalysts: The Role of Intentional and Incidental Iron Incorporation. *J Am Chem Soc* **2014,** *136* (18), 6744-6753, DOI 10.1021/ja502379c.

56. Li, Y.; Zhao, C., Iron-Doped Nickel Phosphate as Synergistic Electrocatalyst for Water Oxidation. *Chem Mater* **2016,** *28* (16), 5659-5666, DOI 10.1021/acs.chemmater.6b01522.

57. Liu, G.; He, D.; Yao, R.; Zhao, Y.; Li, J., Enhancing the water oxidation activity of Ni_2P nanocatalysts by iron-doping and electrochemical activation. *Electrochim Acta* **2017,** *253*, 498-505, DOI 10.1016/j.electacta.2017.09.057.

58. Cheng, F.; Li, Z.; Wang, L.; Yang, B.; Lu, J.; Lei, L.; Ma, T.; Hou, Y., In situ identification of the electrocatalytic water oxidation behavior of a nickel-based metal–organic framework nanoarray. *Mater Horizons* **2021,** *8* (2), 556-564, DOI 10.1039/D0MH01757D.

59. Zhou, J.; Yuan, L.; Wang, J.; Song, L.; You, Y.; Zhou, R.; Zhang, J.; Xu, J., Combinational modulations of $NiSe_2$ nanodendrites by phase engineering and iron-doping towards an efficient oxygen evolution reaction. *J Mater Chem A* **2020,** *8* (16), 8113-8120, DOI 10.1039/d0ta00860e.

TOC

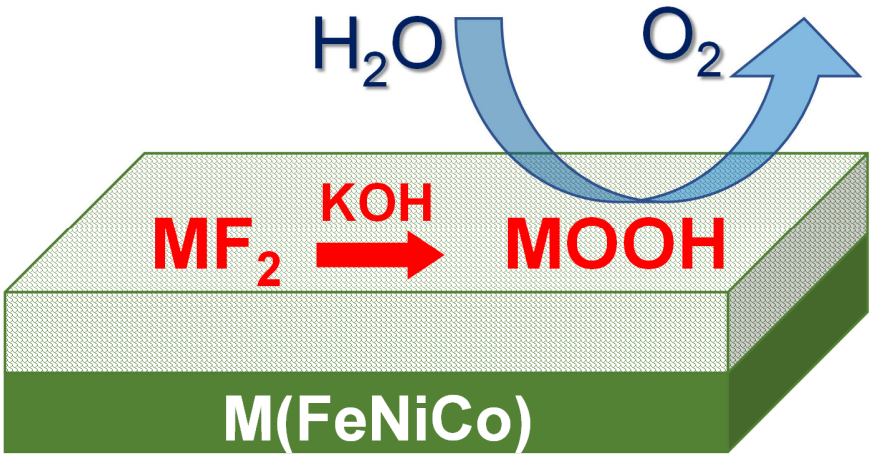

synopsis

A highly active FeNiCo oxyhydroxide OER electrode is formed directly from the $(FeNiCo)F_2$ layer formed by anodizing.